ARTICLE

doi:10.1038/nature24452

Tidal tomography constrains Earth's deep-mantle buoyancy

Harriet C. P. Lau[1], Jerry X. Mitrovica[1], James L. Davis[2], Jeroen Tromp[3], Hsin-Ying Yang[4,5] & David Al-Attar[6]

Earth's body tide—also known as the solid Earth tide, the displacement of the solid Earth's surface caused by gravitational forces from the Moon and the Sun—is sensitive to the density of the two Large Low Shear Velocity Provinces (LLSVPs) beneath Africa and the Pacific. These massive regions extend approximately 1,000 kilometres upward from the base of the mantle and their buoyancy remains actively debated within the geophysical community. Here we use tidal tomography to constrain Earth's deep-mantle buoyancy derived from Global Positioning System (GPS)-based measurements of semi-diurnal body tide deformation. Using a probabilistic approach, we show that across the bottom two-thirds of the two LLSVPs the mean density is about 0.5 per cent higher than the average mantle density across this depth range (that is, its mean buoyancy is minus 0.5 per cent), although this anomaly may be concentrated towards the very base of the mantle. We conclude that the buoyancy of these structures is dominated by the enrichment of high-density chemical components, probably related to subducted oceanic plates or primordial material associated with Earth's formation. Because the dynamics of the mantle is driven by density variations, our result has important dynamical implications for the stability of the LLSVPs and the long-term evolution of the Earth system.

Earth's elastic structure and its density structure are dominated by spherical symmetry (that is, structure that varies with depth), as captured by seismic reference (or one-dimensional, 1D) models such as PREM[1]. However, from the early 1980s, images of Earth's interior provided by seismic tomography have revealed more complicated structures characterized by laterally varying, percentage-level perturbations in seismic wave speed[2,3]. These perturbations reflect thermal and/or compositional heterogeneity linked to mantle convection, the main driving force for plate tectonics and, more generally, the long-term evolution of the Earth system. Constraining the thermochemical structure of Earth's mantle, and its associated dynamics, remains a key goal in global geophysical research.

Since mantle convection is driven by density variations, or buoyancy, the density field of Earth is a key parameter in constraining the dynamics of mantle flow. Seismic tomographic images show fast wave speed anomalies that spatially correlate with the history of subduction, indicative of mantle that is colder than average, and thus relatively dense, driving downward flow[4,5]. However, the interpretation of slow wave speed anomalies in the form of large-scale domes rising about 1,000 km above the core–mantle boundary (CMB) beneath southern Africa and the Pacific[2,6,7] remains contentious[8].

The debate regarding the LLSVPs (shown in Fig. 1) is mainly based on their net buoyancy. An important complication is that the low seismic wave speeds that characterize the LLSVPs may be due to thermal and/or chemical effects, and thus the buoyancy of the structures derives from some combination of these effects: a hot, thermal anomaly producing positive buoyancy, and compositional heterogeneity (for example, from the enrichment of iron) with an intrinsic negative buoyancy. The uncertainty in the relative contribution of these effects has led to contrasting views of large-scale mantle dynamics: for example, LLSVPs may represent denser than average regions and thus a less energetic mode of mantle convection[6,9–12], or the converse[8,13,14].

With the growing availability of highly precise space-geodetic measurements of crustal deformation, modelling studies[15–19] have begun to explore the information content of tidal observations. Furthermore a recent study has probed 1D Earth structure beneath the western USA using observations of crustal deformation driven by ocean tides[18]. In this Article, we image lower-mantle density variations using a powerful new tomographic procedure—tidal tomography—based on high-precision, GPS-derived observations of Earth's body tide (the tidal deformation of the solid Earth in response to forcings by the Sun and the Moon). Tidal tomography provides an independent constraint on the long-wavelength density and elastic structure of Earth. The methodology is based on a recent theoretical advance in the treatment of Earth's tidal response[20] and our application takes advantage of a dataset comprised of crustal displacement measurements in the semi-diurnal tidal band recorded by a global network of GPS stations with submillimetre-level precision[21]. Tidal deformations are sensitive to deep-mantle, long-wavelength structure (see below) and so our tomographic procedure is uniquely suited to investigating the nature of the LLSVPs.

The symbols in Fig. 1 display the in-phase (with respect to the tidal potential) vertical crustal displacement of the M2 semi-diurnal body tide, corrected for rotational effects, crustal and CMB topography, and 1D density, elastic and anelastic structure[21]. The residual signal is comprised of errors in the above corrections, displacements associated with ocean tidal loading and the perturbation to the body tide response due to lateral variations in mantle elastic and density structure. Constraining the deep, long-wavelength component of the latter structure is the goal of this study. Figure 1 also shows the shear wave speed heterogeneity in the deep mantle (2,800 km depth) according to tomographic model S40RTS[2], and highlights the locations of the two LLSVPs.

We performed preliminary sensitivity analyses that indicated that the body tide response is sensitive to long-wavelength shear wave speed

[1]Department of Earth and Planetary Sciences, Harvard University, Cambridge, Massachusetts, USA. [2]Lamont-Doherty Earth Observatory, Columbia University, New York, USA. [3]Department of Geosciences and Program in Applied and Computational Mathematics, Princeton University, Princeton, New Jersey, USA. [4]Laboratory of Seismology and Physics of Earth's Interior & School of Earth and Space Sciences, University of Science and Technology of China, Hefei, China. [5]National Geophysical Observatory at Mengcheng, University of Science and Technology of China, Anhui, China. [6]Department of Earth Sciences, University of Cambridge, Cambridge, UK.

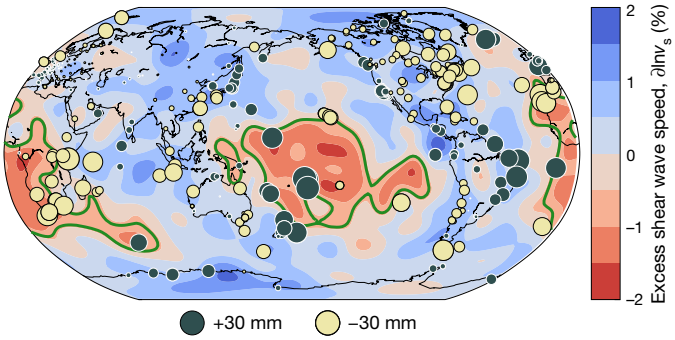

Figure 1 | GPS measurements of vertical M2 body tide deformation[21] overlaying seismic tomographic model S40RTS[2] at a depth of 2,800 km. Circles indicate locations of GPS stations used in this study[21]. The size of the circle is proportional to the amplitude of the in-phase (relative to the tidal potential) vertical displacement associated with the M2 body tide after removing predictions from a 1D density, elastic and anelastic model (PREM[1]) and correcting for crustal[49] and CMB[50] topography (see Methods for details). Dark blue circles indicate positive residuals and yellow circles indicate negative residuals. The underlying contour field displays the shear wave speed (v_s) tomography model S40RTS[2] at 2,800 km depth. The solid green lines mark the boundaries of the two LLSVPs as defined by the 0.65% relative perturbation in shear wave speed[26].

(v_s) and density (ρ) structure in the deepest parts of the mantle and is relatively insensitive to bulk sound speed (v_b) (see Extended Data Fig. 1). To explore this issue further, and to guide the tomographic analysis described below, we performed a second sensitivity analysis designed as follows. First, we adopted variations in v_s within the mantle using one of five seismic tomographic models—GYPSUM[22]; HMSL[23]; S362MANI[24]; S40RTS[2]; or SAW24B16[25]—and scaled these variations in shear wave speed to variations in bulk sound speed using a fixed scaling $R_b = \partial \ln v_b / \partial \ln v_s = 0.05$ (ref. 3). (Note that $\partial \ln X$ denotes the fractional perturbation in parameter X.) Next, we divided the bottom 1,020 km of the mantle into three layers: 'deep' (2,891–2,551 km depth), 'mid' (2,551–2,211 km depth) and 'top' (2,211–1,871 km depth). Across each of these layers we defined two regions: 'LLSVP' and 'outside'. The areal extent of the LLSVP regions in each layer is defined by the −0.65% v_s contour[26] and any region outside the defined margin is considered to be 'outside'. We then perturbed the density in each of the six regions by 5% and computed the perturbation in the M2 body tide response at all sites shown in the GPS network of Fig. 1. This procedure was repeated for each of the five seismic tomographic models.

Figure 2a provides a measure of the sensitivity (defined by the sum of the squares of the perturbed body tide response at all sites) derived from the above calculations. For results based on each seismic tomographic model (shown in each panel in Fig. 2a), the sensitivities are normalized by the largest of the values computed for the six regions. The results show good consistency across the different shear wave tomographic models. This consistency reflects the fact that although the five tomographic models are derived from a wide range of seismic datasets, they have similar long-wavelength structure[27]. In all models the body tide response exhibits peak sensitivity to density perturbations within the deepest layer of the LLSVPs and also substantial sensitivity outside the LLSVPs at this depth. This sensitivity diminishes to negligible levels in the shallowest layer, both inside and outside the LLSVPs, across all models. The GYPSUM, S362MANI and S40RTS models are characterized by sensitivity to perturbations in structure within the middle LLSVPs in the middle layer, while HMSL and SAW24B16 are not. At this middle depth, all models show negligible sensitivity outside the LLSVPs. Figure 2b is a schematic representation of the average sensitivity across all five tomographic models within each of the six spatial regions. From this we reduce our model parameter space to the three regions within which perturbations in density have the greatest impact on the M2 body tide response: deep LLSVP (DL), deep outside (DO) and mid LLSVP (ML). Given the negligible difference between the sensitivity values to both the mid-layer regions (that is, both within and outside the LLSVPs), we additionally performed the following analysis considering the regions DL and DO and the whole mid-layer as a single region. The final conclusions of such a parameterization are consistent with the choice adopted henceforth.

Our inversion procedure is focused on these three regions and is based on a probabilistic approach with a penalty function related to how well a given model prediction correlates with the body tide observations. Specifically, our approach searches for coherence between predictions based on models with laterally varying mantle structure and the large and globally distributed geodetic dataset, and it is particularly suited to noisy datasets. The procedure is as follows: (1) we produce a large dataset by randomly sampling the entire dataset shown in Fig. 1 in accordance with the assigned Gaussian errors associated with each station[21]. Each station is sampled with a frequency that depends on how densely it is clustered with other sites in order to limit bias within the sampled dataset towards data in any single geographic region. Figure 3a (top panel) shows a histogram of residuals after these samples are corrected (see ref. 21) for the body tide prediction based on the 1D elastic, anelastic and density model (we denote these residuals as u_{RAW}); (2) we apply additional corrections associated with Earth rotation (u_{ROT}) and CMB (u_{CMB}) and crustal topographies (u_{CT}). Note that the u_{ROT} correction was provided in ref. 21; and u_{CMB} and u_{CT} have a net signal that is an order of magnitude smaller than the uncertainty in the body tide observations (see Extended Data Fig. 2a and b); (3) a final correction is applied for the response due to the ocean tidal load, u_{OTL}. This correction is performed by randomly drawing u_{OTL} values provided by seven global ocean tide models (see Methods) with the same sampling frequency as that adopted in step (1). We denote the sum of all four corrections listed above as u_{4C}. A histogram of the residuals generated by correcting u_{RAW} for the signals u_{4C} (that is, u_{CORR}, where $u_{CORR} = u_{RAW} - u_{4C}$) is shown in Fig. 3a (bottom panel). The correction for the response to the ocean tidal load is by far the most important, and it leads to a substantial reduction in the spread of the histograms (±35 mm for u_{RAW} to ±6 mm for u_{CORR}), consistent with the findings in ref. 21. (We note that most errors in u_{OTL} are <1 mm, see Extended Data Fig. 2c).

The next three steps in the procedure involve the calculation and assessment of correlations. In particular, we: (4) compute the correlation coefficient, C_0, between the two populations: u_{RAW} and u_{4C}; (5) calculate forward predictions of body tide displacement, $u_{3D}(i)$, for a given three-dimensional (3D) mantle structure model i (removing the contribution from the 1D background model PREM[1]) where we apply all possible combinations of $R_\rho = \partial \ln \rho / \partial \ln v_s$ values in the range $-1 \le R_\rho(\mathrm{DL}) \le 1$, $-1 \le R_\rho(\mathrm{ML}) \le 1$ and $-1 \le R_\rho(\mathrm{DO}) \le 1$ (in increments of 0.05) to a v_s tomographic model randomly drawn from the five listed above. (For the rest of the mantle, we apply the depth-dependent scaling factor[28] shown in Extended Data Fig. 3.) This exercise, which adopts the same sampling frequency at each site as in step (1), yields a set of approximately 10^5 forward predictions. For each forward prediction i, we calculate a new correlation coefficient, $C_1(i)$, between the populations u_{RAW} and $u_{4C} + u_{3D}(i)$, and evaluate whether the additional correction $u_{3D}(i)$ results in a value of $C_1(i)$ for which $C_1(i) > C_0$. Figure 3b shows the histogram of (randomly sampled) Earth models that meet this criterion; finally (6) we assess the statistical significance (see Methods) of each of the models in Fig. 3b. Figure 3c shows the subset of models from Fig. 3b in which $C_1(i)$ exceeds C_0 at the 95% confidence level. In this step, we additionally cull any models that perturb the mean density in any of the three layers by more than 0.5% from the 1D background model.

Distributions of best-performing mantle models

Thirty-four models pass the rotation test at the 95% significance level in Fig. 3c (and Fig. 4a) and to assess whether any bias associated with the five v_s tomographic models exists, we repeated the analysis of Fig. 3c separately for each seismic model (Extended Data Fig. 4). In this

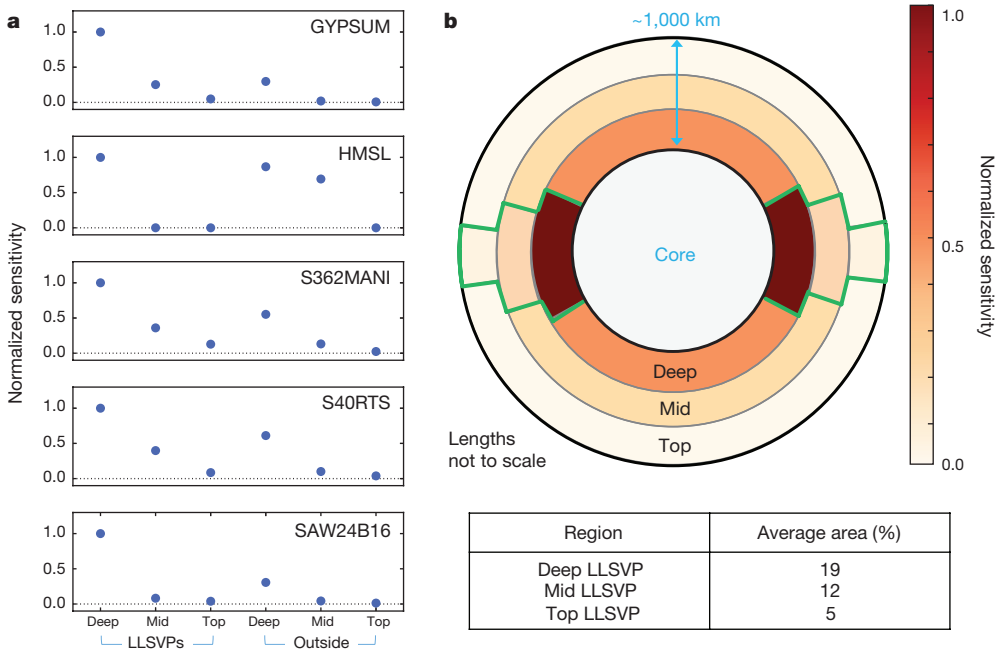

Region	Average area (%)
Deep LLSVP	19
Mid LLSVP	12
Top LLSVP	5

Figure 2 | Sensitivity of body tide measurements to density perturbations in the deep mantle. Analysis of the sensitivity of the body tide response as measured by the global GPS network (Fig. 1) to perturbations in density within the six deep mantle regions defined in the text (deep, mid and top 'LLSVP'; deep, mid and top 'outside'). **a**, Each panel refers to an analysis based on one of the five v_s tomography models described in the text, as labelled[2,22–25]. In each case we compute the sum of the squares of the difference between the 3D and 1D Earth model response, where the former is defined by a 5% perturbation in density across one of the six deep mantle regions, as indicated on the abscissa. The results on each panel are normalized by the greatest of the six root-mean-square differences. Other details of the analysis are described in the text. **b**, A schematic diagram showing the geometry of the six regions considered in the sensitivity analysis, where the colour intensity indicates the average normalized sensitivity across the five v_s tomography models in **a**. The table lists the total areal extent of the LLSVPs within each depth layer.

exercise, we adopted different significance levels for each seismic model so as to generate a comparable number of acceptable models in generating histograms. In particular, the significance level decreases progressively for the seismic models S40RTS, S362MANI, SAW24B16 and HMSL, respectively. (No simulation based on the v_s model of GYPSUM passed the rotation test for statistical significance at a level of 90%.) The histograms in Fig. 3c and Extended Data Fig. 4 show consistent patterns, albeit with varying spreads, across the DL, ML and DO regions, and we conclude that our estimates of R_ρ in Fig. 3c (-0.82 ± 0.11; -0.76 ± 0.20; 0.20 ± 0.07, respectively) and inferences of mean excess density based upon them (Fig. 4a) are robust to the choice of seismic model, where the excess density field is calculated by using

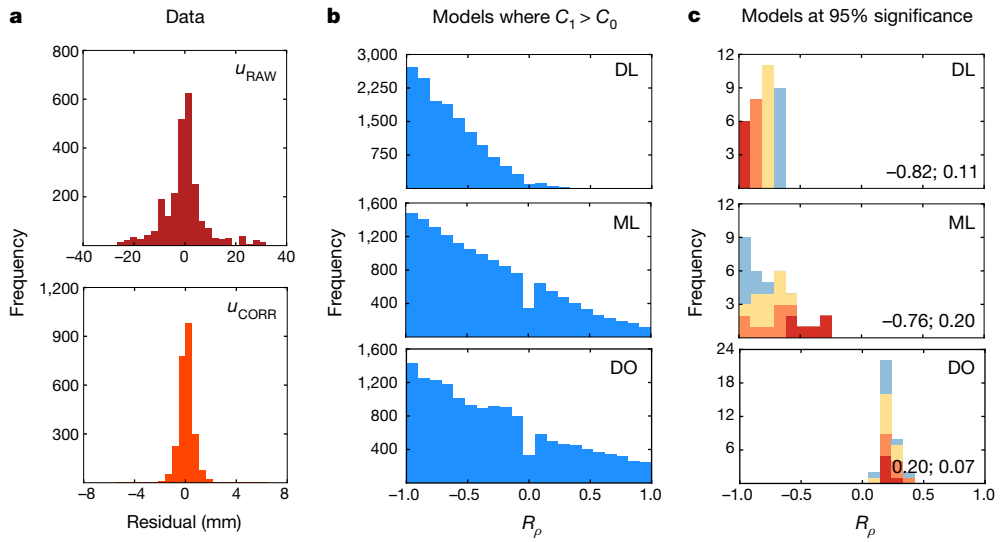

Figure 3 | Histograms of processed GPS data and best-performing mantle models. a, The top panel shows the histogram of the GPS estimates of the in-phase M2 tidal response after correction for the signal computed from an Earth model with the 1D elastic, density and anelastic structure of the PREM Q-model[1] (u_{RAW}). The bottom panel shows the data after applying corrections for the following effects: rotation, crustal and CMB topography and ocean tidal loading (that is, $u_{CORR} = u_{RAW} - u_{4C}$). **b**, Histograms of parameters defining the set of 3D Earth models that yield a correlation coefficient C_1 that exceeds C_0 (see main text). **c**, Histograms of the subset of 3D Earth models in **b** that improve the correlation at the 95% significance level. The colours discretize the range of R_ρ estimates in the top panel and these colours are used to group together subsets of 3D Earth models common to all three panels in **c**. The mean and standard deviation of the distribution are given in each panel.

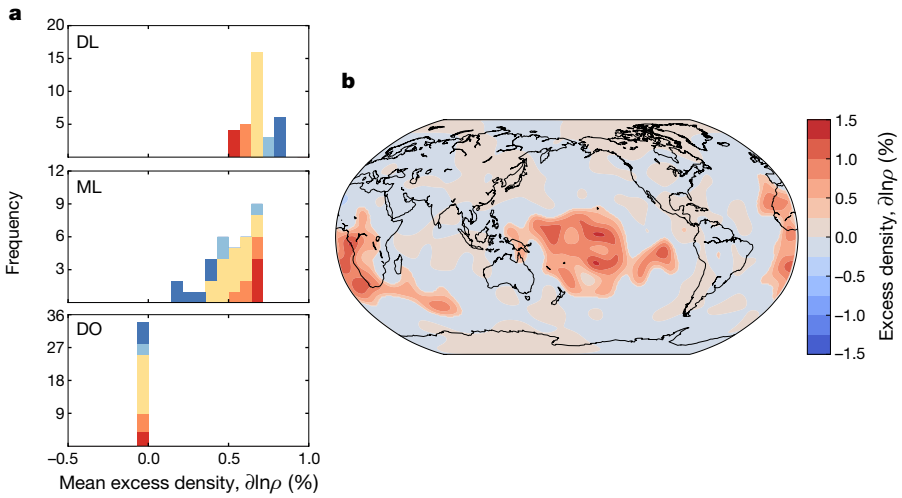

Figure 4 | Histograms of excess densities of best-performing mantle models and the deep mantle excess density field of the mean of these models. a, Histograms of the mean excess density $<\partial \ln \rho>$ in each region for the models shown in Fig. 3c. The colours discretize the range of the excess density $<\partial \ln \rho>$ estimates in the top panel and they are used to group together subsets of the 3D Earth models common to all three panels. Note that the colours here are unrelated to those in Fig. 3c. **b**, The density field across the deepest mantle layer (extending to 350 km above the CMB) computed by applying the mean values of R_ρ(DL) and R_ρ(DO) in the top and bottom panels of Fig. 3c to the shear wave tomography model S40RTS[2].

the R_ρ value of choice and multiplying this by the v_s anomaly ($\partial \ln v_s$) field of a given seismic model. (Additional tests we performed indicate that the uncertainty for R_ρ(DO) should be doubled to conservatively account for potential errors in the geocentre correction applied to the GPS data.) We note that there is some correlation between the spread in the histograms in Extended Data Fig. 4 and the sensitivity analysis of Fig. 2a. For example, the accepted models for layer ML and model SAW24B16 have a wide range relative to the other results in Extended Data Fig. 4; this is consistent with the weak sensitivity of body tide measurements to density structure in this layer when this particular seismic v_s model is adopted (Fig. 2a). Thus, the inference summarized in Fig. 4a is dominated by simulations adopting the tomographic models S40RTS and S362MANI.

Figure 4a shows histograms of the mean excess density within the three mantle regions DL, ML and DO, computed using each of the solutions summarized in Fig. 3c. The median values on each histogram are 0.67%, 0.54% and −0.03%, with interquartile ranges of 0.61% to 0.74%, 0.44% to 0.64% and −0.04% to −0.02%, respectively. We conclude, on the basis of these GPS-based constraints on the M2 body tide, that the integrated excess density within the lowest 700 km or so of the LLSVPs has a median value of 0.60% and an interquartile range of 0.56% to 0.62%. This result indicates that high-density chemical components within these large-scale deep-mantle regions dominate thermal effects in establishing their integrated buoyancy. An example of the inferred density field within the deepest mantle layer (comprising regions DO and DL) derived from one of the models in Fig. 3c, with R_ρ values of $R_\rho(\mathrm{DL}) = -0.82$, $R_\rho(\mathrm{ML}) = -0.72$ and $R_\rho(\mathrm{DO}) = -0.20$, applied to seismic tomographic model S40RTS, is shown in Fig. 4b.

To gain deeper insight into the statistical significance of the above estimates, we performed a series of tests to explore the resolving power of the body tide data. To begin, we repeated the calculations of Extended Data Fig. 1 at much finer depth discretization, focusing on perturbations of spherical harmonic degree 2 and degree 3 structure (Extended Data Fig. 5). The smooth increase of sensitivity with depth of these kernels is characterized by a length scale that is broader than the thickness of our model layers, and this indicates that estimates associated with regions DL and ML must, at some level, be correlated (or, more precisely, anti-correlated). This notion is supported by an inversion we performed in which we computed synthetic body tide data using a mantle with R_ρ values of $R_\rho(\mathrm{DL}) = -0.50$, $R_\rho(\mathrm{ML}) = 0.1$ and $R_\rho(\mathrm{DO}) = 0.05$ (Extended Data Fig. 6). The histograms of R_ρ(DL) and R_ρ(ML) indicate that estimates across these two regions are indeed anti-correlated, though mildly (correlation coefficient −0.52). In an additional test of this type, we performed an inversion of synthetic data computed using a mantle model in which the region DL was divided into two layers: a 100-km-thick layer at the CMB and an overlying layer of thickness 250 km. We imposed R_ρ values of −0.8 and 0.1 in these two layers, as well as R_ρ(ML) and R_ρ(DO) values of 0.1 and 0.15, respectively. Results from this test (Extended Data Fig. 7) indicate that the body tide data cannot resolve structure with a spatial scale smaller than the thickness of the DL layer. Thus, we cannot discount the possibility that our estimates of the excess density in the DL layer reflect structure of smaller scale than the DL layer situated at the very base of the mantle.

Implications for LLSVP stability and mantle dynamics

Supporting evidence for the existence of compositional heterogeneity within the mantle comes from a variety of sources, including geochemical analyses of mantle-derived rocks[29], where potential sources of different chemical reservoirs include subducted oceanic lithosphere[30], unprocessed mantle material (that is, mantle untouched by melt extraction at the surface)[31], and residual material from a differentiation event early in Earth's history[9]. Numerical simulations of thermochemical mantle convection indicate that relatively dense compositional heterogeneity may accumulate naturally within deep-mantle regions, or piles[32], and that the morphology of such regions is consistent with LLSVP geometries when realistic plate subduction histories are incorporated into the modelling[8,33]. Laboratory experiments exploring convection in a chemically stratified mantle suggest that the LLSVPs may instead reflect an oscillatory doming regime, much like that observed in a lava lamp, that operates when density contrasts are less than 1% (ref. 34), a value consistent with our derived bounds on the excess density in these structures (Fig. 4a). These bounds are also consistent with numerical "mixing" experiments[35,36] which indicate that excess densities of order 1% are required to preserve chemical heterogeneity over billion-year timescales.

A global inversion of seismic normal mode splitting data, augmented by geodynamic modelling of long-wavelength free-air gravity anomalies[6], implied an anti-correlation between v_s and ρ (that is, negative R_ρ values) at the base of the mantle. The spatial resolution of such studies was subsequently questioned[37]. However, a recent inversion[12] of a large database of seismic records, including updated normal splitting functions, surface wave phase anomalies, body wave travel times, and long-period waveforms, implied an excess density of approximately 1%

at the base of the mantle, roughly coincident with the location of the LLSVPs, consistent with the results in ref. 6. Nevertheless, the adoption of the self-coupling approximation of normal mode theory in both these seismic studies may have introduced inaccuracies in the inference of structure[38–40]. (Our methodology does not adopt the self-coupling approximation; see Methods for a more detailed discussion.) Many seismological studies[3,41] also report anti-correlation between v_b and v_s within the LLSVPs, a result that implies compositional heterogeneity[42]. Moreover, an analysis of a set of SKS phases traversing the eastern flank of the African LLSVP has suggested that this boundary has a relatively sharp (about a 3% drop in shear wave speed across 50 km) gradient in wave speed, consistent with a dense chemical layer bordered by an upwelling thermal structure[43,44]. More recently, however, an analysis of a class of normal modes known as Stoneley modes (characterized by heightened sensitivity along and near the CMB) indicates that LLSVPs are characterized by positive integrated buoyancy[45]. However, the data cannot exclude the possibility of a thin (about 100 km) region of negative buoyancy at the base of the mantle.

Notwithstanding the above studies, the relative effects of chemistry and temperature on the buoyancy of the LLSVPs has been a source of much debate. As an example, a combined analysis of seismic, geodynamic and mineral physics data within the framework of viscous flow modelling concluded that while the LLSVPs are characterized by compositional heterogeneity relative to the surrounding mantle, they are, in bulk, buoyant and actively upwelling[14]. In addition, recent thermochemical flow modelling[8] has suggested that many seismic observations that have been used to argue that LLSVPs are denser than the surrounding mantle—this includes the anti-correlation between v_b and v_s within the LLSVPs and the sharp gradient in shear wave speed at the edge of the African LLSVP discussed above, as well as the large amplitude of the shear wave speed anomaly and the high ratio of shear-to-compressional wave speed within the structures[42,46]—are also consistent with a model in which the LLSVPs are buoyant structures. In particular, it is possible that the anti-correlation between v_b and v_s may reflect the existence of a post-perovskite phase[47,48] at the base of the LLSVPs and that the large amplitudes and gradients in v_s may be explained by considering the effects of temperature- and pressure-dependent anelasticity[28].

Although these arguments do indicate non-unique results in the inference of compositional heterogeneity within the deep mantle, they cannot explain our inferred anti-correlation[42] between v_s and ρ (Fig. 3c); our conclusion that the LLSVPs are, on average, denser than the surrounding mantle is therefore robust. Future work in developing tidal tomography, including the incorporation of seismic measurements of body tides and the analysis of other (diurnal and long-period) tidal bands, will refine our bounds on buoyancy within Earth's deep mantle, and thus further improve our understanding of mantle flow and its role in the evolution of the Earth system.

Online Content Methods, along with any additional Extended Data display items and Source Data, are available in the online version of the paper; references unique to these sections appear only in the online paper.

Received 24 March; accepted 22 September 2017.

1. Dziewonski, A. M. & Anderson, D. L. Preliminary reference Earth model. *Phys. Earth Planet. Inter.* **25,** 297–356 (1981).
2. Ritsema, J., Deuss, A., van Heijst, H. J. & Woodhouse, J. H. S40RTS: a degree-40 shear-velocity model for the mantle from new Rayleigh wave dispersion, teleseismic traveltime and normal-mode splitting function measurements. *Geophys. J. Int.* **184,** 1223–1236 (2011).
3. Masters, G., Laske, G., Bolton, H. & Dziewonski, A. M. The relative behavior of shear velocity, bulk sound speed, and compressional velocity in the mantle: implications for chemical and thermal structure. *Geophys. Monogr.* **117,** 63–87 (2000).
4. Van der Hist, R., Engdahl, R., Spakman, W. & Nolet, G. Tomographic imaging of subducted lithosphere below northwest Pacific island arcs. *Nature* **353,** 37–43 (1991).
5. Zhao, D. Global tomographic images of mantle plumes and subducting slabs: insight into deep Earth dynamics. *Phys. Earth Planet. Inter.* **146,** 3–34 (2004).
6. Ishii, M. & Tromp, J. Normal-mode and free-air gravity constraints on lateral variations in velocity and density of Earth's mantle. *Science* **285,** 1231–1236 (1999).
7. Masters, G., Laske, G., Bolton, H. & Dziewonski, A. The relative behavior of shear velocity, bulk sound speed, and compressional velocity in the mantle: implications for chemical and thermal structure. In *Earth's Deep Interior: Mineral Physics and Tomography From the Atomic to the Global Scale* (eds Karato, S.-I., Forte, A., Liebermann, R., Masters, G. & Stixrude, L.) Geophys. Monogr. Ser. 117 (American Geophysical Union, 2000).
8. Davies, D. R. *et al.* Reconciling dynamic and seismic models of Earth's lower mantle: the dominant role of thermal heterogeneity. *Earth Planet. Sci. Lett.* **353,** 253–269 (2012).
9. Kellogg, L. H. Compositional stratification in the deep mantle. *Science* **283,** 1881–1884 (1999).
10. Tackley, P. J. Strong heterogeneity caused by deep mantle layering. *Geochem. Geophys. Geosyst.* **3,** https://doi.org/10.1029/2001GC000167 (2002).
11. Trampert, J., Deschamps, F., Resovsky, J. & Yuen, D. Probabilistic tomography maps chemical heterogeneities throughout the lower mantle. *Science* **306,** 853–856 (2004).
12. Moulik, P. & Ekström, G. The relationships between large-scale variations in shear velocity, density, and compressional velocity in the Earth's mantle. *J. Geophys. Res. Solid Earth* **121,** 2737–2771 (2016).
13. Hager, B. H., Clayton, R. W., Richards, M. A., Comer, R. P. & Dziewonski, A. M. Lower mantle heterogeneity, dynamic topography and the geoid. *Nature* **313,** 541–545 (1985).
14. Forte, A. M. & Mitrovica, J. X. Deep-mantle high-viscosity flow and thermochemical structure inferred from seismic and geodynamic data. *Nature* **410,** 1049–1056 (2001).
15. Dehant, V., Defraigne, P. & Wahr, J. M. Tides for a convective Earth. *J. Geophys. Res.* **104,** 1035 (1999).
16. Métivier, L. & Conrad, C. P. Body tides of a convecting, laterally heterogeneous, and aspherical Earth. *J. Geophys. Res.* **113,** B11405 (2008).
17. Latychev, K., Mitrovica, J. X., Ishii, M., Chan, N.-H. & Davis, J. L. Body tides on a 3-D elastic earth: toward a tidal tomography. *Earth Planet. Sci. Lett.* **277,** 86–90 (2009).
18. Ito, T. & Simons, M. Probing asthenospheric density, temperature, and elastic moduli below the western United States. *Science* **332,** 947–951 (2011).
19. Qin, C., Zhong, S. & Wahr, J. A perturbation method and its application: elastic tidal response of a laterally heterogeneous planet. *Geophys. J. Int.* **199,** 631–647 (2014).
20. Lau, H. C. P. *et al.* A normal mode treatment of semi-diurnal body tides on an aspherical, rotating and anelastic Earth. *Geophys. J. Int.* **202,** 1392–1406 (2015).
21. Yuan, L., Chao, B. F., Ding, X. & Zhong, P. The tidal displacement field at Earth's surface determined using global GPS observations. *J. Geophys. Res. Solid Earth* **118,** 2618–2632 (2013).
22. Simmons, N. A., Forte, A. M., Boschi, L. & Grand, S. P. GyPSuM: A joint tomographic model of mantle density and seismic wave speeds. *J. Geophys. Res.* **115,** B12310 (2010).
23. Houser, C., Masters, G., Shearer, P. & Laske, G. Shear and compressional velocity models of the mantle from cluster analysis of long-period waveforms. *Geophys. J. Int.* **174,** 195–212 (2008).
24. Kustowski, B., Ekström, G. & Dziewoński, A. M. Anisotropic shear-wave velocity structure of the Earth's mantle: a global model. *J. Geophys. Res.* **113,** B06306 (2008).
25. Mégnin, C. & Romanowicz, B. The three-dimensional shear velocity structure of the mantle from the inversion of body, surface and higher-mode waveforms. *Geophys. J. Int.* **143,** 709–728 (2000).
26. Torsvik, T. H., Smethurst, M. A., Burke, K. & Steinberger, B. Large igneous provinces generated from the margins of the large low-velocity provinces in the deep mantle. *Geophys. J. Int.* **167,** 1447–1460 (2006).
27. Lekic, V., Cottaar, S., Dziewonski, A. & Romanowicz, B. Cluster analysis of global lower mantle tomography: A new class of structure and implications for chemical heterogeneity. *Earth Planet. Sci. Lett.* **357,** 68–77 (2012).
28. Karato, S. Importance of anelasticity in the interpretation of seismic tomography. *Geophys. Res. Lett.* **20,** 1623 (1993).
29. Hofmann, A. W. Mantle geochemistry: the message from oceanic volcanism. *Nature* **385,** 219–229 (1997).
30. Christensen, U. R. & Hofmann, A. W. Segregation of subducted oceanic crust in the convecting mantle. *J. Geophys. Res.* **99,** 19867 (1994).
31. Allègre, C. J., Hofmann, A. & O'Nions, K. The argon constraints on mantle structure. *Geophys. Res. Lett.* **23,** 3555–3557 (1996).
32. Tackley, P. J. in *The* Core-Mantle *Boundary Region* (eds Gurnis, M., Wysession, M. E., Knittle, E. & Buffett, B. A.) 231–253 (American Geophysical Union, 1998).
33. McNamara, A. K. & Zhong, S. Thermochemical structures beneath Africa and the Pacific Ocean. *Nature* **437,** 1136–1139 (2005).
34. Davaille, A. Simultaneous generation of hotspots and superswells by convection in a heterogeneous planetary mantle. *Nature* **402,** 756–760 (1999).
35. Nakagawa, T. & Tackley, P. J. Effects of thermo-chemical mantle convection on the thermal evolution of the Earth's core. *Earth Planet. Sci. Lett.* **220,** 107–119 (2004).
36. Brandenburg, J. P., Hauri, E. H., van Keken, P. E. & Ballentine, C. J. A multiple-system study of the geochemical evolution of the mantle with force-balanced plates and thermochemical effects. *Earth Planet. Sci. Lett.* **276,** 1–13 (2008).

37. Kuo, C. & Romanowicz, B. On the resolution of density anomalies in the Earth's mantle using spectral fitting of normal-mode data. *Geophys. J. Int.* **150,** 162–179 (2002).
38. Deuss, A. & Woodhouse, J. H. Theoretical free-oscillation spectra: the importance of wide band coupling. *Geophys. J. Int.* **146,** 833–842 (2001).
39. Al-Attar, D., Woodhouse, J. H. & Deuss, A. Calculation of normal mode spectra in laterally heterogeneous Earth models using an iterative direct solution method. *Geophys. J. Int.* **189,** 1038–1046 (2012).
40. Yang, H.-Y. & Tromp, J. Synthetic free-oscillation spectra: an appraisal of various mode-coupling methods. *Geophys. J. Int.* **203,** 1179–1192 (2015).
41. Su, W. & Dziewonski, A. M. Simultaneous inversion for 3-D variations in shear and bulk velocity in the mantle. *Phys. Earth Planet. Inter.* **100,** 135–156 (1997).
42. Karato, S. & Karki, B. B. Origin of lateral variation of seismic wave velocities and density in the deep mantle. *J. Geophys. Res.* **106,** 21771–21783 (2001).
43. Ni, S., Tan, E., Gurnis, M. & Helmberger, D. Sharp sides to the African superplume. *Science* **296,** 1850–1852 (2002).
44. Sun, D., Tan, E., Helmberger, D. & Gurnis, M. Seismological support for the metastable superplume model, sharp features, and phase changes within the lower mantle. *Proc. Natl Acad. Sci. USA* **104,** 9151–9155 (2007).
45. Koelemeijer, P., Deuss, A. & Ritsema, J. Density structure of Earth's lowermost mantle from Stoneley mode splitting observations. *Nat. Commun.* **8,** 15241 (2017).
46. Brodholt, J. P., Helffrich, G. & Trampert, J. Chemical versus thermal heterogeneity in the lower mantle: the most likely role of anelasticity. *Earth Planet. Sci. Lett.* **262,** 429–437 (2007).
47. Murakami, M., Hirose, K., Kawamura, K., Sata, N. & Ohishi, Y. Post-perovskite phase transition in $MgSiO_3$. *Science* **304,** 855–858 (2004).
48. Wookey, J., Stackhouse, S., Kendall, J.-M., Brodholt, J. & Price, G. D. Efficacy of the post-perovskite phase as an explanation for lowermost-mantle seismic properties. *Nature* **438,** 1004–1007 (2005).
49. Laske, G., Masters, G., Ma, Z. & Pasyanos, M. Update on CRUST1.0—a 1-degree global model of Earth's crust. *Geophys. Res. Abstr.,* **15,** EGU2013–2658 (2013).
50. Mathews, P. M., Herring, T. A. & Buffett, B. A. Modeling of nutation and precession: new nutation series for nonrigid Earth and insights into the Earth's interior. *J. Geophys. Res.* **107,** 2156–2202 (2002).

Acknowledgements H.C.P.L. and J.X.M. acknowledge support from NSF CSEDI grant EAR-1464024, NASA grant NNX17AE42G, and Harvard University. J.L.D. was supported in part by NASA grant NNX17AD97G. H.-Y.Y. was supported by the Chinese Academy of Sciences under grant number XDB18010304 and 2015TW1ZB0001. H.C.P.L. thanks J. Austermann for performing mantle convection simulations during the review process.

Author Contributions H.C.P.L. led the development of the body tide theory, the numerical/statistical analysis of GPS measurements of semi-diurnal body tides reported in the literature, and the writing of the manuscript. J.X.M. contributed to the statistical analysis and interpretation of the results while J.L.D. contributed algorithms to calculate tidal amplitudes and investigated potential impacts of GPS orbit errors. J.T., D.A.-A., H.-Y.Y. and J.X.M. contributed to the development of the body tide theory and numerical software. All these authors contributed text to the manuscript.

Author Information Reprints and permissions information is available at www.nature.com/reprints. The authors declare no competing financial interests. Readers are welcome to comment on the online version of the paper. Publisher's note: Springer Nature remains neutral with regard to jurisdictional claims in published maps and institutional affiliations. Correspondence and requests for materials should be addressed to H.C.P.L. (harrietlau@fas.harvard.edu).

Reviewer Information *Nature* thanks L. Métivier, B. Romanowicz and the other anonymous reviewer(s) for their contribution to the peer review of this work.

METHODS

Forward modelling of body tides. To predict the semi-diurnal body tide response we use a fully coupled normal-mode perturbation theory that accounts for the effects of rotation, topography on discontinuities, and lateral elastic/anelastic and density structure[20]. Note that the full coupling of normal modes is distinct from the approach adopted in previous seismic data analyses, which have invoked approximate methods of normal mode coupling[6,12]. The self-coupling approximation, in particular, substantially degrades the accuracy of predictions of the body tide response[20]; similar concerns regarding accuracy have been raised in the application of self-coupling to the seismic normal mode problem[38–40].

Our methodology adopts the normal modes of a 1D Earth (PREM[1]) as a basis set, and, in the presence of the effects listed, calculates the coupling between these modes. After considering many synthetic tests, we have chosen to fully couple the following set of modes: $\{{}_0S_2, {}_2S_1, {}_0S_3, {}_0S_4, {}_1S_2, {}_0S_0, {}_0S_5, {}_1S_3, {}_2S_2, {}_0S_6, {}_3S_2, {}_1S_4, {}_2S_3, {}_2S_4, {}_1S_0, {}_4S_2\}$. We note that other modes, including toroidal modes, have a minor and undetectable effect on the vertical component of the body tide response. An example of a prediction of the M2 body tide response is provided in Extended Data Fig. 8a, which shows the residual (3D minus 1D) amplitude of the in-phase (with respect to the tidal potential) vertical displacement. This particular calculation adopts the v_s tomographic model S40RTS[2]. Density perturbations are prescribed by applying the depth-dependent scaling shown in Extended Data Fig. 3 (ref. 28) and perturbations in bulk sound speed are computed from the shear wave model using a fixed value of R_b of 0.05 (ref. 3).

In analogy to the seismic normal-mode problem, the sensitivity of body tide predictions to lateral variations in structure is largest for perturbations characterized by even spherical harmonic degrees. Extended Data Fig. 8b shows, across our full suite of 3D Earth models, the power spectrum of the density field within the deepest layer, DL. Each bar represents the largest contribution at a given spherical harmonic degree across all our models, normalized by the largest value across all spherical harmonic degrees. A dominant signal is evident at spherical harmonic degree 2. This result, combined with the even-degree sensitivity described above and the spherical harmonic degree 2 (sectorial) geometry of the semi-diurnal forcing, indicates that body tide observations are particularly well suited to constraining the long-wavelength structure of Earth's deep mantle.

Data processing. We use a published dataset comprised of Earth's in- and out-of-phase crustal deformation associated with several semi-diurnal and diurnal tidal constituents[21], as measured by 456 globally distributed GPS stations (Fig. 1). Our analysis uses only the in-phase vertical component of the M2 body tide, the largest semi-diurnal tidal constituent, and GPS-based estimates are corrected for the following effects: (1) the rotation of Earth (which is already applied in ref. 21); (2) the crustal topography using the crustal model CRUST1.0[49]; and (3) the excess ellipticity (that is, the non-hydrostatic ellipticity) of the CMB[50]. Although CMB topography is uncertain[51], the excess ellipticity component of this topography is accurately known[50]. Nevertheless, results of several tests summarized in Extended Data Fig. 2 demonstrate that the GPS-derived body tide data are insensitive to the CMB excess ellipticity and crustal topography relative to the uncertainty of the GPS measurements. Corrections (2) and (3) are applied using the normal-mode perturbation theory[20] described above. Finally, all values of u_{RAW} considered in the analysis are residuals, and so are corrected for the background 1D elastic, density and anelastic structure of Earth, as described in ref. 21. All observations and predictions are taken relative to a reference site located in Williams Lake, Canada (we chose this site owing to its very small observational uncertainty).

As we have noted, the focus of this study is the 3D elastic and density structure of Earth. The question arises as to the possible sensitivity of our results to Earth's 3D anelastic structure. Very little is known in regard to this structure. 1D anelasticity has an approximately 1% effect on the in-phase response of the body tide[52]. 3D anelasticity is likely to introduce a perturbation of the order of 1% to this signal (that is, around 0.01% overall). We conclude that 3D anelasticity will produce an in-phase signal that is an order of magnitude beneath the level of detection of our data. The impact of 3D anelasticity on the out-of-phase component of the body tide response will be much larger and for this reason the present analysis considers only the in-phase component of the M2 tidal constituent.

Ocean tidal loading. To isolate the signature of 3D mantle elastic and density structure, the final effect to be removed from the GPS estimates is the deformation associated with M2 ocean tidal loading, which has the same frequency as the M2 body tide. As part of our statistical tests, we considered u_{OTL} calculated from seven global ocean tidal models (NAO99[53], FES2004[54], TPX2010[55], TPX2011[55], DTU[56], EOT[57], HAMTIDE[58]) and randomly sample from these. To calculate the deformation signal, u_{OTL}, associated with each of these models, we adopt PREM[1] (both the continental and oceanic lithosphere versions) and use the software package SPOTL[59]. We do not consider the impact of 3D structure on the ocean tide response for two reasons: (1) the implementation of a correction based on 3D structure would be difficult owing to the high resolution that is required at coastlines in order to compute these effects accurately; and (2) the ocean tidal loading signal is primarily sensitive to structure in the uppermost upper mantle[18], which, as demonstrated by Extended Data Fig. 1, has little impact on the body tide response. Hence, any deep mantle 3D structure we adopt in our analysis of the body tide will have negligible effect on the ocean tidal response. The effect of shallow 3D structure is accounted for by implementing the different versions of upper-mantle PREM structure in the SPOTL software. We also note that the standard deviation in the ocean tidal loading correction across the seven ocean tidal models is relatively low at most of the sites used in this study (see Extended Data Fig. 2c).

The original study that provided GPS estimates of the M2 body tide displacement found that measurements using sites near the coast (defined as lying within 150 km of the ocean) were characterized by large uncertainties in the ocean tidal loading corrections[21]. To assess whether the inclusion of data from such sites substantially affected our conclusions we repeated the statistical analysis summarized in Fig. 3c with a reduced dataset involving 'inland' sites (sites at least 150 km away from a coastline). This reduced the total number of sites adopted in the analysis from 456 to 135. The results, summarized in Extended Data Fig. 9, indicated that our conclusions based on an analysis of the full body tide dataset are relatively insensitive to the accentuated errors in the OTL corrections at coast sites. The histograms in Extended Data Fig. 9 are broader than those in Fig. 3c, reflecting the reduced information content of the inland-site dataset.

Statistical tests. The expanded dataset required for our statistical tests is constructed by randomly sampling GPS estimates at each site (accounting for Gaussian errors in these estimates[21]) with a frequency proportional to a site's cumulative squared distance from other sites. We normalize this number such that the maximum number of samples for any site is 10,000. This approach results in a dataset of 2,457,122 measurements with a mean sampling number of 5,388. We note that in the test for correlations described below we remove outliers that can be explained only by unmodelled noise. This results in the removal of about 4% of the total dataset.

As we note in the main text, we compute the correlation, C_0, between the raw GPS dataset u_{RAW} and the set of corrections for Earth rotation, CMB and crustal topographies, and ocean tidal loading (which sum to u_{4C}). We then add an additional correction for the signal due to the 3D elastic and density structure and re-compute the correlation C_1. By considering a large number of 3D Earth models we derive the set $C_1(i)$ and retain only those models for which $C_1(i)>C_0$. We can denote this smaller set as $C_1(i^*)$.

In the event that the GPS-based estimates from each sampled set were uncorrelated, establishing the statistical significance of the difference between a given C_1 in the set $C_1(i^*)$ and C_0 would involve a standard statistical test (for example, the Student's t-test). However, this is not the case in our analysis. Accordingly, to assess statistical significance we adopt the following approach. For each model that improves C_0, that is, the set i^* of all 3D models and their associated predicted body tide displacements $u_{3D}(i^*)$, we perform 1,000 random rotations of the predicted body tide displacement field of that model. For each rotation (which we denote by the index j) we sample the field at the location of the GPS sites, yielding $u_{3DR}(i^*,j)$. Then, for a given 3D Earth model in the set i^*, we calculate a new correlation coefficient, $C_{3DR}(i^*,j)$, between the two populations u_{CORR} ($= u_{RAW} - u_{4C}$) and $u_{3DR}(i^*,j)$, resulting in a different set of 1,000 values of $C_{3DR}(i^*,j)$, where $j = 1, 2,..., 1,000$. This random distribution serves as our null hypothesis. We then calculate a single correlation coefficient, $C_{3D}(i^*)$, between the following populations, u_{CORR} and $u_{3D}(i^*)$. We consider a model $u_{3D}(i^*)$ to be statistically significant at the percentile for which it lies within the distribution of $C_{3DR}(i^*,j)$, where $j = 1, 2,..., 1,000$. Extended Data Fig. 10 provides two examples of the application of this test, one in which a model reaches the 95% significance level and one where it does not. In the successful case, the geographical variation of the displacement field shows a level of coherence with respect to the GPS-based measurements beyond that which can be explained by merely reproducing the spatial wavelengths captured by observation.

Data availability. The GPS data that support the findings of this study are available within the supplementary information files provided in ref. 21.

Code availability. Computer codes used to produce these results will be made available upon request to the corresponding author.

51. Koelemeijer, P. J., Deuss, A. & Trampert, J. Normal mode sensitivity to Earth's D″ layer and topography on the core-mantle boundary: what we can and cannot see. *Geophys. J. Int.* **190,** 553–568 (2012).
52. Wahr, J. & Bergen, Z. The effects of mantle anelasticity on nutations, Earth tides, and tidal variations in rotation rate. *Geophys. J. Int.* **87,** 633–668 (1986).
53. Matsumoto, K., Takanezawa, T. & Ooe, M. Ocean tide models developed by assimilating TOPEX/POSEIDON altimeter data into hydrodynamical model: a global model and a regional model around Japan. *J. Oceanogr.* **56,** 567–581 (2000).
54. Lyard, F., Lefevre, F., Letellier, T. & Francis, O. Modelling the global ocean tides: modern insights from FES2004. *Ocean Dyn.* **56,** 394–415 (2006).
55. Egbert, G. D., Erofeeva, S. Y., Egbert, G. D. & Erofeeva, S. Y. Efficient inverse modeling of barotropic ocean tides. *J. Atmos. Ocean. Technol.* **19,** 183–204 (2002).

56. Cheng, Y. & Andersen, O. B. Improvement in global ocean tide model in shallow water regions. Poster SV.1-68 *OST-ST Meeting on Altimetry for Oceans and Hydrology, Lisbon.* (2010).
57. Savcenko, R. & Bosch, W. EOT11a—empirical ocean tide model from multi-mission satellite altimetry. DGFI Technical Report No. 89 (Deutsches Geodätisches Forschungsinstitut (DGFI), 2012).
58. Taguchi, E., Stammer, D. & Zahel, W. Inferring deep ocean tidal energy dissipation from the global high-resolution data-assimilative HAMTIDE model. *J. Geophys. Res. Oceans* **119,** 4573–4592 (2014).
59. Agnew, D. C. NLOADF: a program for computing ocean-tide loading. *J. Geophys. Res. Solid Earth* **102,** 5109–5110 (1997).
60. Li, X.-D., Giardini, D. & Woodhouses, J. H. Large-scale three-dimensional even-degree structure of the Earth from splitting of long-period normal modes. *J. Geophys. Res.* **96,** 551 (1991).
61. Morelli, A. & Dziewonski, A. M. Topography of the core–mantle boundary and lateral homogeneity of the liquid core. *Nature* **325,** 678–683 (1987).
62. Sze, E. K. M. & van der Hilst, R. D. Core mantle boundary topography from short period PcP, PKP, and PKKP data. *Phys. Earth Planet. Inter.* **135,** 27–46 (2003).

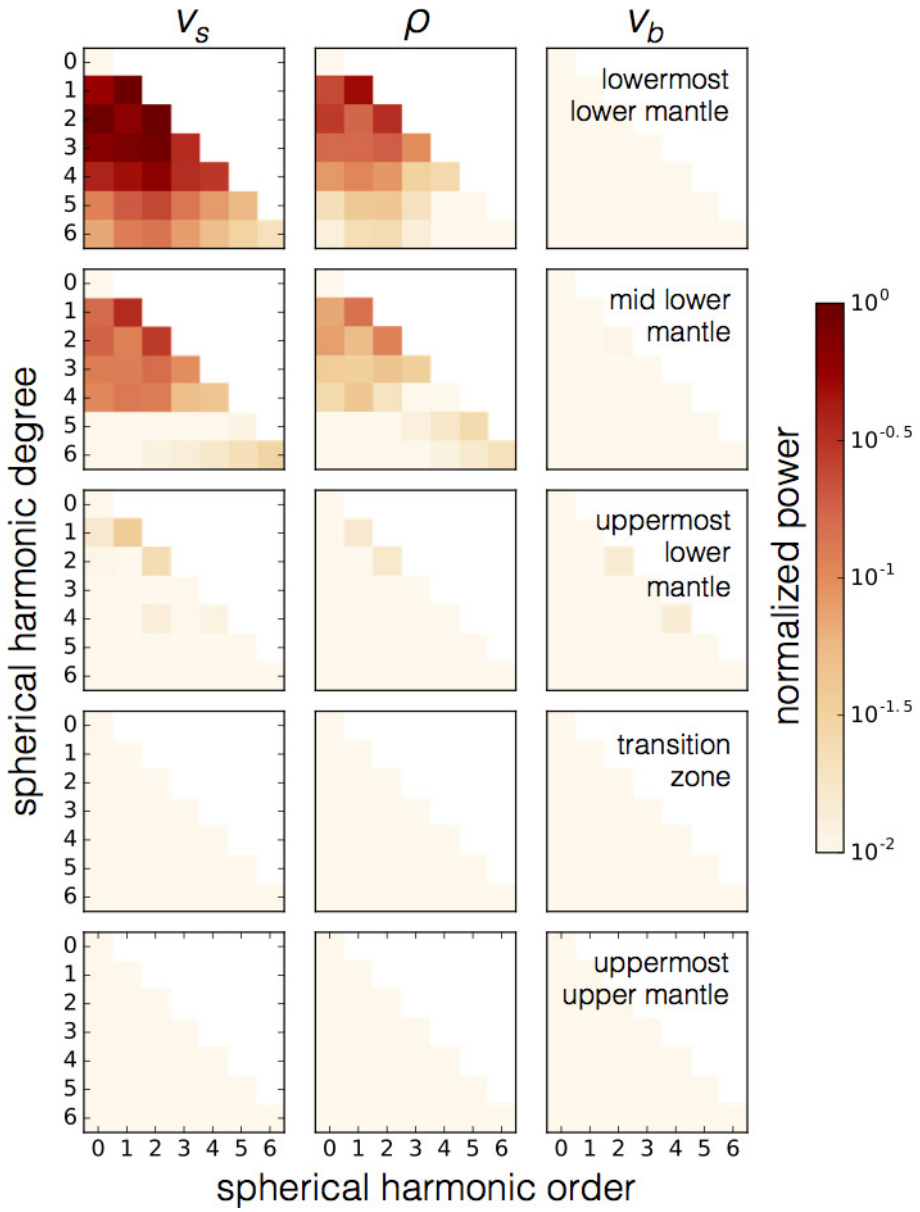

Extended Data Figure 1 | Sensitivity of the body tide response to wave speed and density perturbations throughout the mantle. The sensitivity of the computed semi-diurnal body tide response to perturbations in shear wave speed v_s (left column), density ρ (middle column), and bulk sound speed v_b (right column) structure. Perturbations to structure are applied in five layers throughout the mantle (from top row to bottom row): lowermost lower mantle (2,891–2,211 km depth); mid lower mantle (2,211–1,201 km depth); uppermost lower mantle (1,201–670 km depth); transition zone (670–400 km depth); and uppermost upper mantle (400–24 km). The perturbations are expressed in terms of normalized power and decomposed into spherical harmonic coefficients up to degree and order 6. We define the normalized power as the total sum of the squared residual (3D minus 1D Earth model).

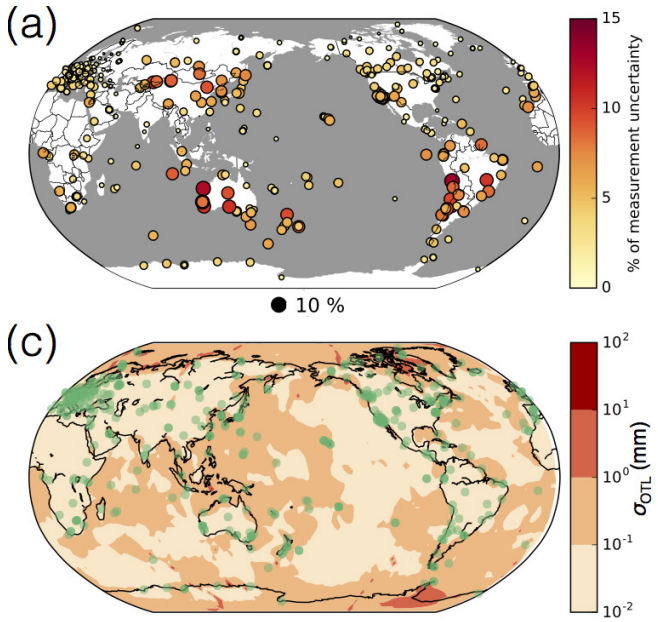

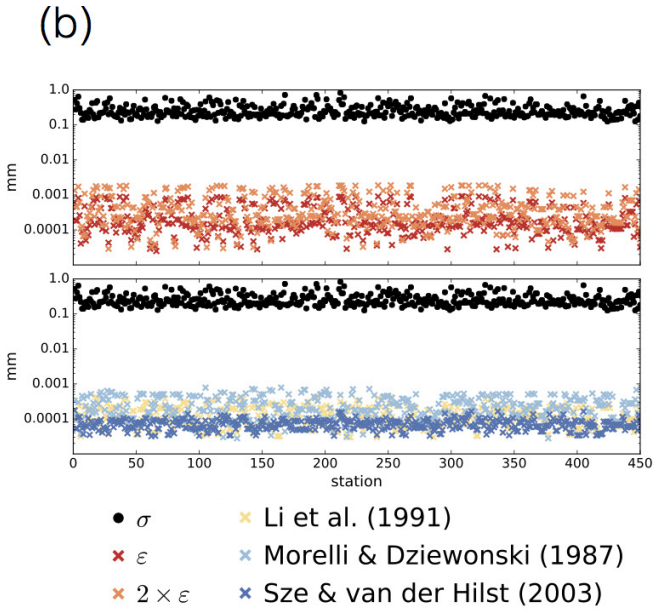

Extended Data Figure 2 | Effects of crustal and CMB topography, and ocean tidal loading on GPS body tide measurements. a, Crustal[49] and CMB topography[50] corrections to the body tide response (see Methods) shown as a percentage of the measurement uncertainty in the GPS data[21]. The magnitude of the corrections is indicated by both the size and colour intensity of the circles. **b**, The vertical axis refers to two quantities, denoted by crosses and black circles: (1) perturbations to u_{3D} at each station when five different CMB topography models are imposed, all denoted by crosses. The symbol ε denotes the perturbation computed from the CMB excess ellipticity model adopted in the main text[50] and the remaining results (yellow, light-blue and dark-blue crosses) are based on topography models estimated from seismic observations[60–62]; (2) the uncertainty in the GPS measurements (σ, denoted by black circles). All perturbations to u_{3D} (crosses) are of much lower amplitude than σ (black circles). **c**, The standard deviation, σ_{OTL}, of a set of predictions of vertical crustal displacement associated with ocean loading, u_{OTL}, computed using the seven ocean tide models described in the Methods section. The green circles mark the locations of the GPS sites use in our analysis.

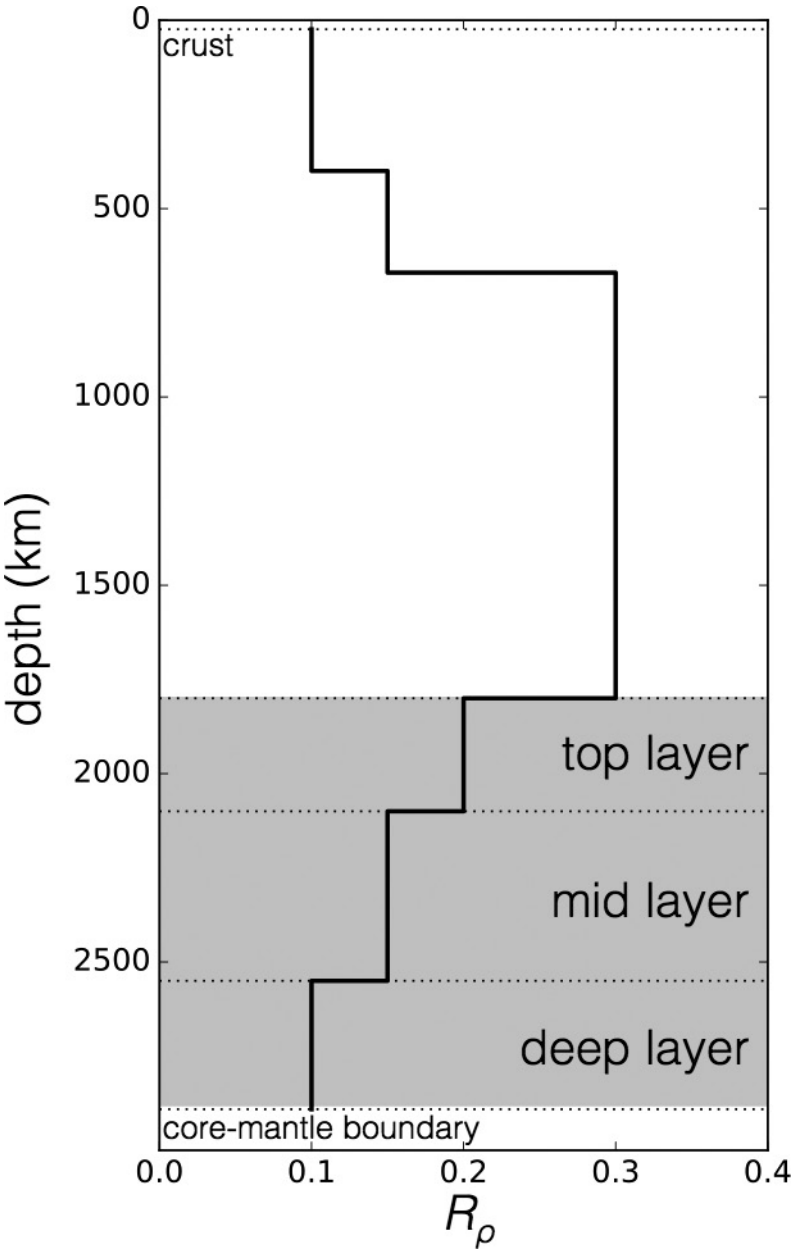

Extended Data Figure 3 | Depth-dependent v_s-to-density scaling[28] adopted in this study. Radial dependence of the scaling factor R_ρ, applied (within the shallowest three layers of our Earth models) to convert perturbations in shear wave speed v_s to perturbations in density[28] ρ. The scaling factors within the lowest three regions (shaded) are treated as free parameters in the analyses described in the text.

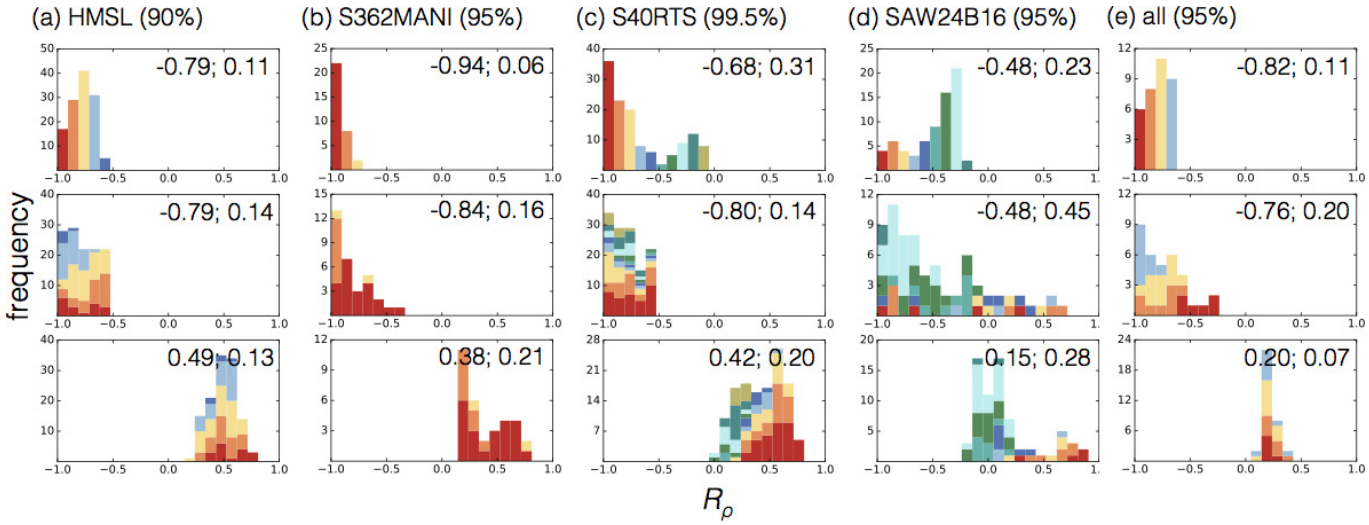

Extended Data Figure 4 | Histograms of best-performing mantle models when adopting single tomographic models. Statistical tests performed as in Fig. 3c of the main text, but considering only a single seismic model listed in turn: **a**, HMSL[23], **b**, S362MANI[24], **c**, S40RTS[2], **d**, SAW24B16[25] and **e**, all (as in Fig. 3c). In each column, the top, middle and bottom panels correspond to regions DL, ML and DO, respectively. The statistical significance of each of these tests is given in parentheses above each column. Values listed in the top right corner of each of these panels are the mean and the standard deviations of the distributions.

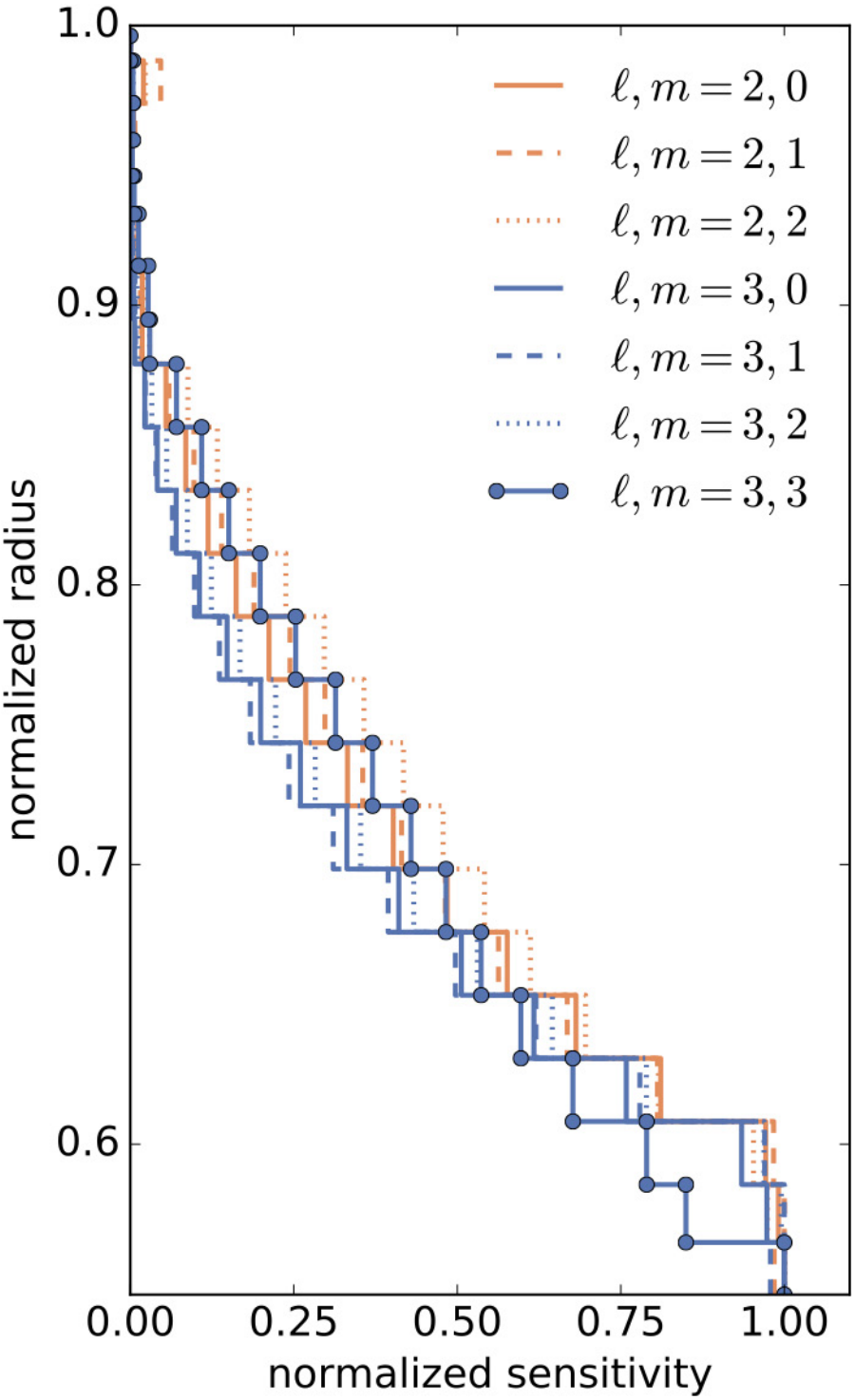

Extended Data Figure 5 | Depth sensitivity of body tide response to long wavelength density perturbations. Depth sensitivity of body tide response to density perturbations of spherical harmonic degree *l* and order *m* throughout the mantle. 'Normalized sensitivity' represents the sum of the squared residuals of the vertical amplitude of the body tide at the GPS sites used in this study, where the maximum is scaled to 1.

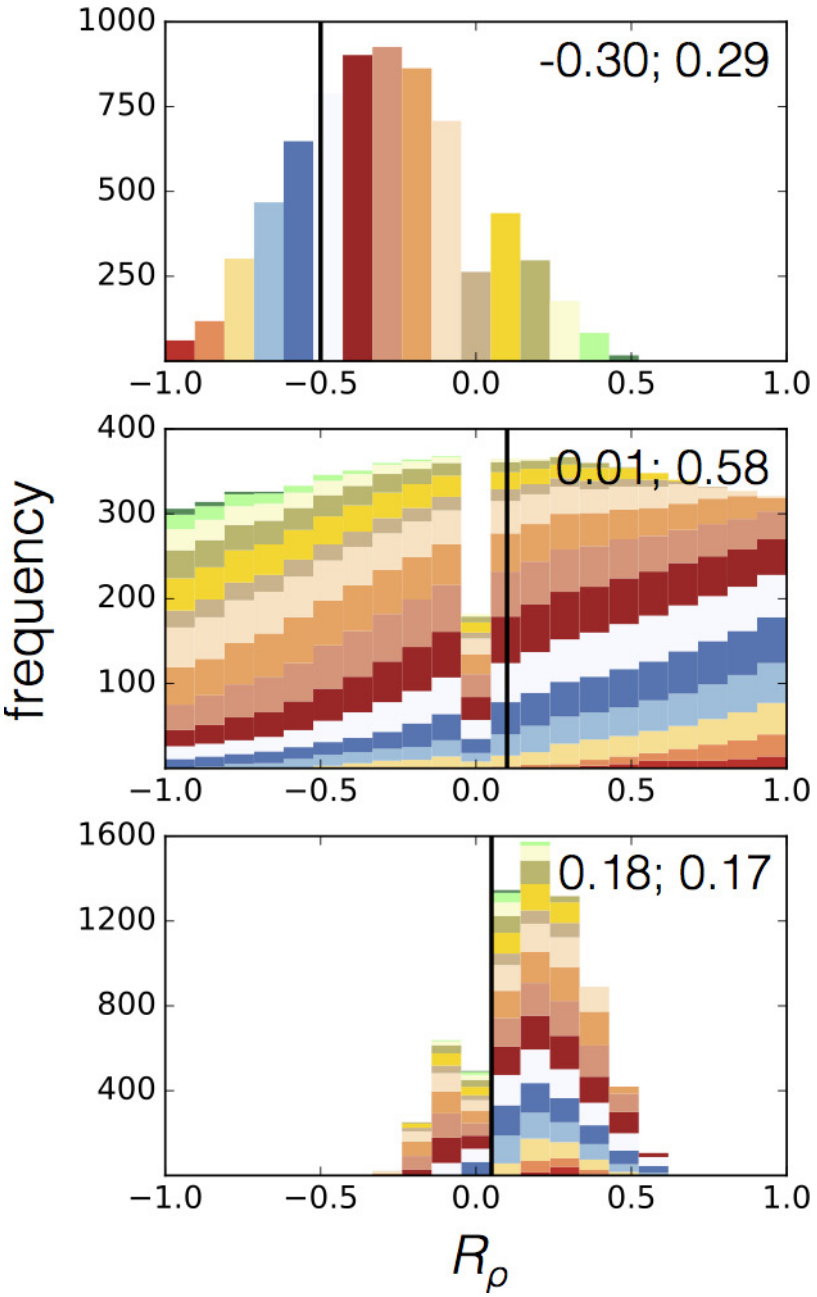

Extended Data Figure 6 | Results from synthetic inversion to test correlations between the deep and mid LLSVP regions. A synthetic inversion analogous to the calculations performed to produce Fig. 3c. Here, synthetic 'observations' of the body tide are produced by adopting the seismic model S40RTS[2] and imposing a mantle structure where $R_\rho(\mathrm{DL}) = -0.5$; $R_\rho(\mathrm{ML}) = 0.1$; and $R_\rho(\mathrm{DO}) = 0.05$ (as shown by the black vertical line on each panel). The top, middle and bottom panels correspond to regions DL, ML and DO, respectively. The posterior estimate and standard deviation for each parameter is listed on the associated panel. The colours discretize the range of R_ρ estimates in the top panel and these colours are used to group together subsets of 3D Earth models common to all three panels. In characterizing the synthetic data, we adopted the same uncertainty as reported in the original GPS dataset by ref. 21.

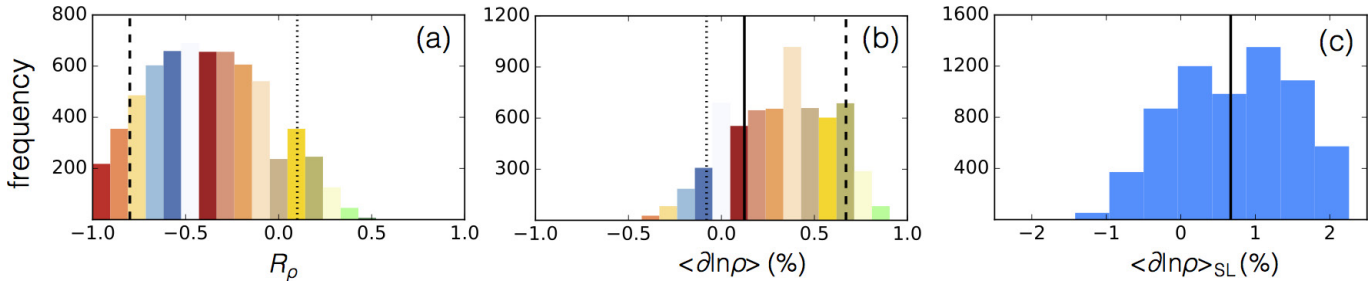

Extended Data Figure 7 | Results from synthetic inversion to test the effect of a dense, thin layer at the base of the mantle. A synthetic inversion analogous to the calculations performed to produce Fig. 3c. Histograms are shown for estimates of the parameter R_ρ(DL) (**a**), and the associated mean excess density $<\partial\ln\rho>_{DL}$ (**b**). The synthetic data are computed by adopting the seismic model S40RTS[2], R_ρ(ML) = +0.1 and R_ρ(DO) = +0.15. The DL layer used in the synthetics is comprised of a 100-km-thick sub-layer (that is, at the base of the mantle) with an R_ρ value of −0.8 (dashed black line in **a**) and a 250-km-thick top layer with R_ρ = +0.1 (dotted black line in **a**). The mean excess densities associated with these two layers are $<\partial\ln\rho>_{SL}$ = 0.7% and $<\partial\ln\rho>_{TL}$ = −0.1% (dashed and dotted black lines in **b**), respectively. The solid black line indicates the mean excess density across the whole DL region, $<\partial\ln\rho>_{DL}$. **c**, The distribution of our estimated $<\partial\ln\rho>_{SL}$ from **b**, after correcting for the weighted sensitivity (see text). The true $<\partial\ln\rho>_{SL}$ (that is, the value used to compute the synthetic data, 0.7%) is marked by the solid vertical black line.

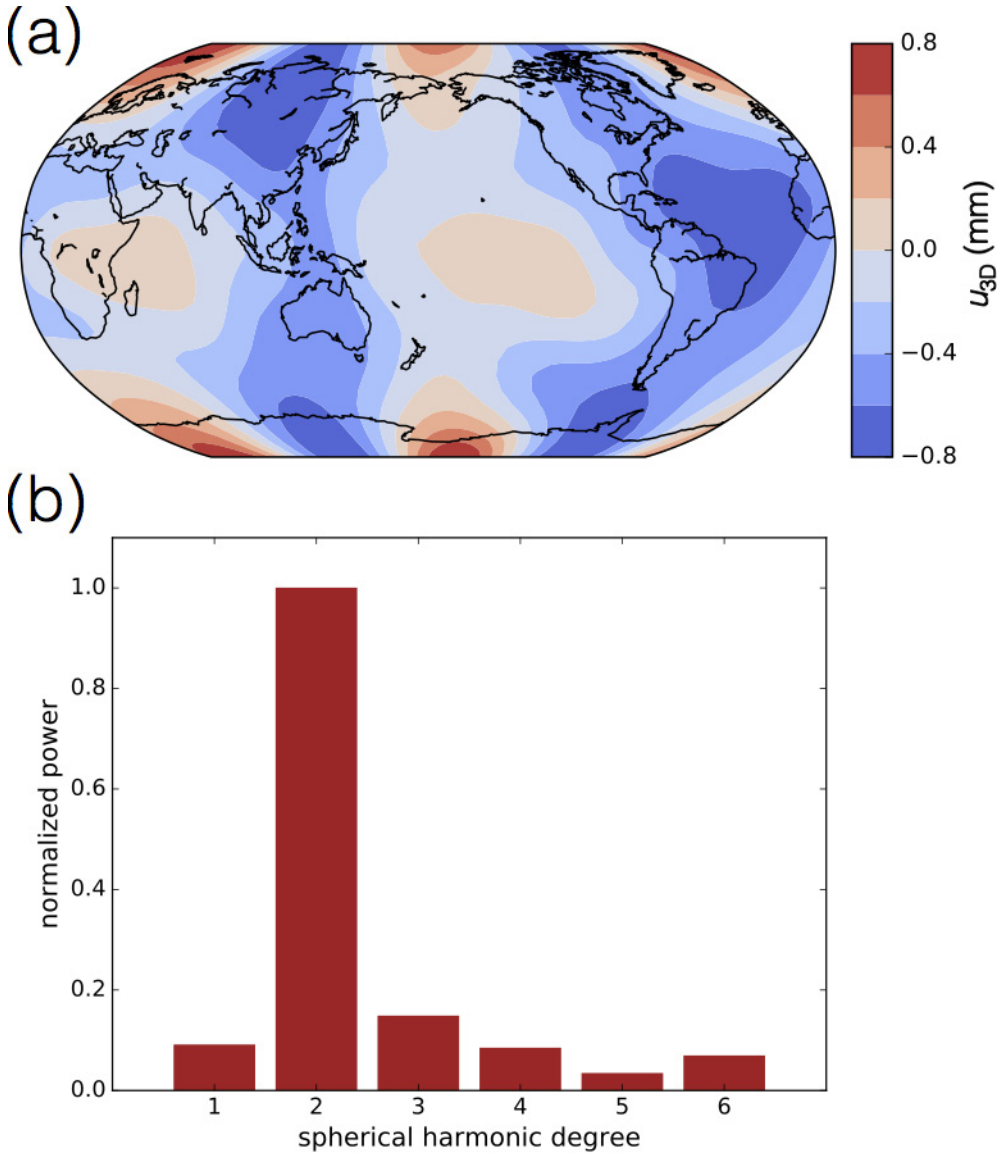

Extended Data Figure 8 | Example of body tide deformation field and spectral characteristics of seismic tomographic models in the deep mantle. a, Difference in the amplitude of the in-phase vertical displacement of the semi-diurnal body tide predicted using 3D and 1D Earth models. The underlying mantle structure is that of S40RTS[2], scaled to perturbations in bulk sound speed v_b (as discussed in the main text) and to perturbations in ρ by applying the scaling factors shown in Extended Data Fig. 3. **b**, A combined power spectrum of the density field of the deep layer, DL, across the entire suite of 3D models tested. Each bar represents the maximum power across all models at the associated spherical harmonic degree. The values on the histogram are normalized using the maximum power across all models and all degrees (which occurs at spherical harmonic degree 2).

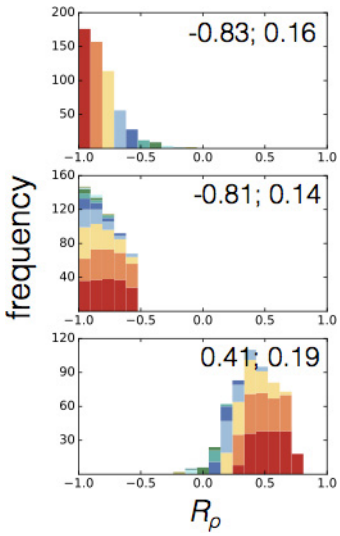

Extended Data Figure 9 | Repeat inversion using only GPS stations away from coastlines. Statistical tests performed as in Fig. 3c except that only a subset of GPS sites are used. In this calculation we use only inland sites (defined as being at least 150 km away from the nearest coastline, as in ref. 21). This reduces the number of sites from 456 to 135. The top, middle and bottom panels correspond to regions DL, ML and DO, respectively. The values listed in the top right corner of each panel are the mean and standard deviations of the associated distributions.

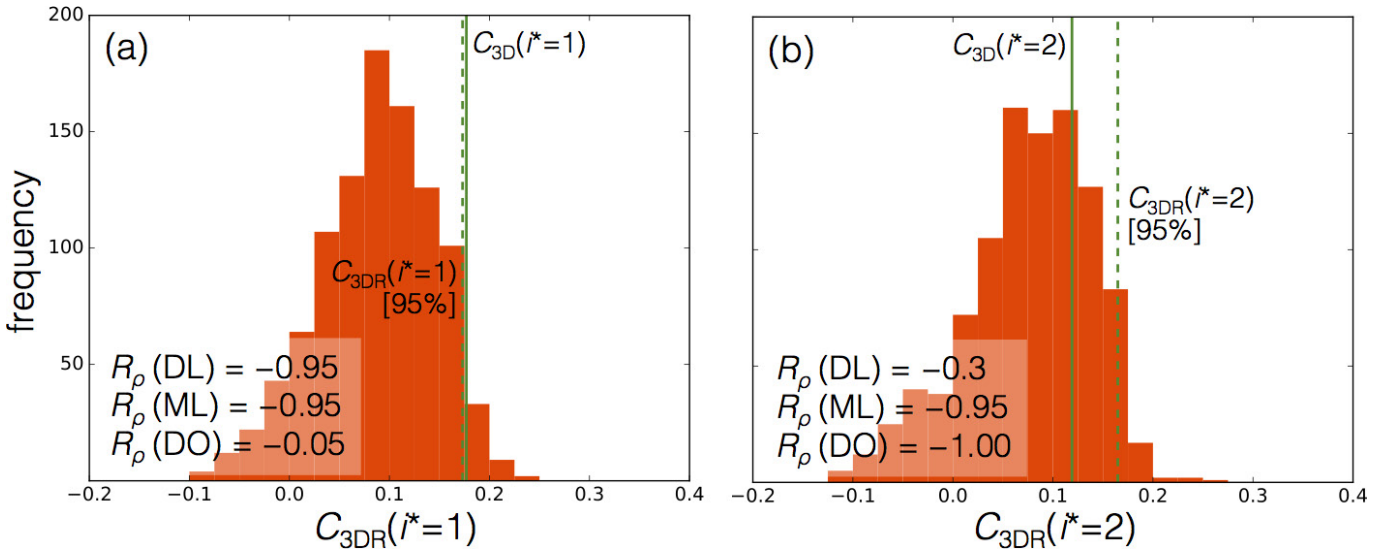

Extended Data Figure 10 | Example histograms resulting from rotation tests. Testing the statistical significance level of two different 3D Earth models ($i^* = 1$ or 2) for which $C_1(i^*) > C_0$ (as defined in the text). Each panel corresponds to a different 3D Earth model (constructed with the R_ρ values listed in the inset) and shows the histogram of $C_{3DR}(i^*, j)$ (where $j = 1, 2,.., 1{,}000$) values produced by rotating the predicted field (see Methods). The dashed green line shows the 95% level of these histograms and the solid green line shows $C_{3D}(i^*)$ for the given 3D Earth model. In **a**, $C_{3D}(i^* = 1)$ exceeds the 95% confidence level and thus passes the statistical significance test; in contrast, in **b** $C_{3D}(i^* = 2)$ fails this test.